SSC24-VI-03

Miniaturized scintillation based detector for characterizing energetic electron precipitation

Anant Telikicherla
University of Alberta
Edmonton, Alberta, Canada, T6G2R3
anant.telikicherla@ualberta.ca

Faculty Advisors: Robert Fedosejevs[1], Ian R. Mann[2]
University of Alberta
Edmonton, Alberta, Canada, T6G2R3
[1]rfed@ualberta.ca, [2]imann@ualberta.ca

ABSTRACT

In-situ measurements of energetic particle precipitation in the near-Earth space environment are essential for understanding the governing physical processes responsible for this precipitation, as well as to elucidate the possible impacts of space radiation on the Earth's atmosphere. In this study, we present the design of a novel miniaturized detector to measure energetic electron precipitation. The detector is one of the instruments to be flown on-board the Canadian RADiation Impacts on Climate and Atmospheric Loss Satellite (RADICALS) mission, which is a low-Earth orbiting satellite planned to launch in 2026/2027. The detector is optimized to measure high energy electron microburst precipitation, which is believed to be caused by bursty and short timescale (< 1 second) scattering of electrons from the Van Allen belts into the Earth's atmosphere. Despite their short timescales, microbursts are thought to cause a significant loss of energetic electrons from the Van Allen belts during geomagnetic storms and also considerably impact the atmospheric chemistry through the generation of NOx/HOx which in-turn can cause Ozone destruction in the mesosphere and upper stratosphere. However, because of limitations in current space instrumentation pertaining to time resolution and energy range, measurements made to date have not been able to conclusively answer many open questions regarding microburst precipitation. In this study, we introduce the RADICALS mission concept with emphasis on energetic particle precipitation (and in particular microburst) measurements. The detector (referred to as the Microburst Detector (MBD)) to be flown on-board the RADICALS mission, aims to obtain high temporal resolution in-situ measurements of microburst precipitation over a broad energy range. The design of the MBD is explained in detail, which is a Multi-Pixel Photon Counter (Silicon Photomultiplier) based scintillation detector that can resolve sub-relativistic and relativistic microbursts with energies between 200 keV and 3 MeV at 10 ms cadence. The MBD has been designed with a modular architecture enabling use on future CubeSats, Balloons, Sounding Rockets and Small Satellite missions. The initial version of this detector has also been developed as part of the Payload for Energetic Particle Precipitation Education and Research (PEPPER-X) project, which is the first Canadian student team experiment selected to launch on-board the NASA RockSat-X sounding rocket mission in August 2024. In this paper, we also summarize the detector design and calibration tests performed for the sounding rocket test flight. Successful operation on this sounding rocket platform would raise the Technology Readiness Level (TRL) of the detector and electronics, paving the way for its use on-board the RADICALS mission and other small satellite missions.

Introduction

The near-Earth space environment comprises of regions of energetic charged particles known as the Van Allen radiation belts. There are predominantly two belts, the inner and outer, with the outer radiation belt primarily consisting of electrons and inner belt primarily consisting of protons.[1] The electron population in the outer belt is highly dynamic and shows variability across a wide energy range and on multiple time scales ranging from minutes, days to years.[2,3] Even though the radiation belts were discovered by James Van Allen over half a century ago,[4] the various physical processes responsible for the variability in the radiation environment are not yet completely understood.

Studying the various loss and acceleration processes causing the dynamics of the near-Earth space radiation environment are important for a variety of reasons. Firstly, energetic electron precipitation (EEP) from the magnetosphere into the Earth's atmosphere can also play an important role in the Earth's climate system. Understanding the impact of energetic electron precipitation on the Earth's atmosphere and climate, for example through the catalytic destruction of ozone in the middle atmosphere by NOx and HOx,[5] remains an active area of Magnetosphere-Ionosphere-Thermosphere (MIT) coupling studies. Furthermore, these energetic charged particles, pose considerable risks to both astronauts and spacecraft avionics.[6] As humanity prepares to return to the moon in the coming years through the Artemis program, a thorough understanding of the radiation environment becomes imperative for effective mission planning. Knowledge of the radiation environment is essential for devising appropriate shielding measures against this space radiation, ensuring the safety of astronauts and the nominal operation of spacecraft subsystems. In this study, we present the design and realization of a novel instrument to characterize energetic electron precipitation from a small-satellite platform to answer some of these open questions in radiation belt physics. The next section provides an overview of the EEP process, and describes the current measurement methodologies and existing gaps.

Background: Current EEP measurement methodologies

Figure 1 (a) shows a pictorial representation the EEP process, as well as different ground-based and space-based methods of characterizing EEP. The figure shows a representative energetic electron moving along a magnetic field line of the Earth. Due to the Earth's dipole magnetic field, electrons perform periodic bounce motion between "Mirror Points". The mirror point of the particle (the location where the particle reverses its parallel velocity) is defined by the location where the local pitch angle (angle between the electron's velocity vector and the local magnetic field, denoted by α in Fig. 1(a)) reaches 90 degrees. If the mirror point falls below a certain altitude range (approx. 100 km), the electron interacts with the atmosphere and is subsequently lost. The maximum pitch angle within which the electron is lost to the atmosphere is known as the local loss cone. Energetic electron precipitation is known to occur when radiation belt electrons are scattered into the local loss cone, due to wave-particle interactions with plasma waves in the equatorial region[7] (denoted by 1 in Figure 1 (a)).

Energetic electron precipitation can be studied using Ground-Based measurements (through all sky imagers, riometers etc), balloon-based measurements of Bremsstrahlung X-rays produced by precipitating electrons,[8] sounding rocket measurements, and in-situ electron measurements in space. Among these methods, in-situ measurements using satellites in the low-Earth orbit provides an ideal platform for energetic electron precipitation measurements. This is because as the energetic electrons travel along the magnetic field lines, the local loss cone angle increases as shown in figure 1. Thus, precipitating particles can be resolved accurately as compared to satellites at the equatorial region. Multiple low Earth orbit missions ranging from CubeSats (For example FIREBIRD-II,[9] AeroCube-6,[10] ELFIN[11]) as well as small satellites (For example SAMPEX[12]) have measured energetic electron precipitation.

However, due to limitations in instrumentation pertaining to energy range, temporal resolution, and directionality, these measurements to date have not been able to definitely answer questions pertaining to EEP. One particular form of energetic electron loss that has recently been the subject of many studies in the space physics community is Microburst precipitation. These represent bursty and short timescale (< 1 s) scattering of energetic (few keV to MeV) electrons from the Van Allen belts into the Earth's atmosphere. Open questions include (a) What is the energy spectrum of electron microbursts? (b) Do low-energy (100s keV) and relativistic (few MeV) microbursts occur simultaneously? (c) What is the contribution of microburst precipitation to the overall precipitation budget? and (d) What is the spatial extent of microbursts i.e. are they localised over a small region or spread over a larger region? (See[7] and references therein, for a detailed summary of the current understanding and open questions pertaining to microburst precipitation). Thus, more extensive additional extensive measurements of microbursts are required to better understand their impact on atmospheric chemistry, and their role as a potentially significant radiation belt loss mechanism.

The RADICALS Mission Concept

To bridge the gaps in the existing measurements and address the open scientific question pertaining to microburst precipitation, we are developing a novel miniaturized detector that will make high temporal and energy resolution measurements of electron microbursts. The detector is being designed to fly

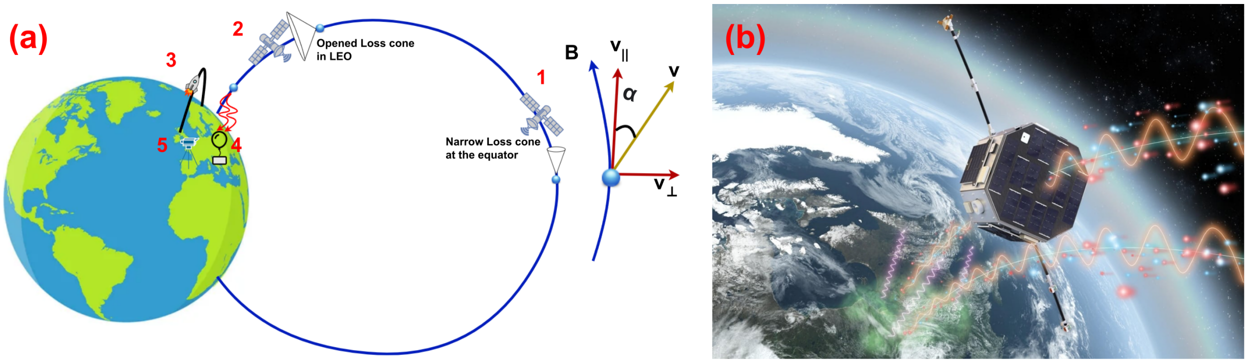

Figure 1: (a) Different ways to measure particle precipitation: (1) In-situ electron measurements in the radiation belts, (2) In-situ measurements in low Earth orbit, (3) In-situ measurements using sounding rockets, (4) Remote sensing using balloon based measurements of Brehmstrallung X-rays, (5) Remote sensing using ground-based instruments (e.g., all-sky imagers, riometers etc). (b) Artistic rendition of the RADICALS mission, showing the low Earth orbiting satellite measuring precipitating electrons, back-scattered Bremsstrahlung X-rays, and plasma wave signatures (Right Image Credit: Andy Kale, Dept. of Physics, University of Alberta).

on-board the *RADiation Impacts on Climate and Atmospheric Loss Satellite (RADICALS)* mission that will investigate the transport of space radiation into the atmosphere. The RADICALS mission is planned to launch in a low-Earth polar orbit ($\approx$ 500-600 km altitude) and utilizes a spin-stabilized configuration, spinning with a nominal period of 30 seconds, which enables the instruments in the payload to monitor full directionality and energy spectrum of the precipitating particles. Figure 1 (b) shows an artistic rendition of the RADICALS mission. For in-situ characterization of precipitating radiation, the satellite consists of a telescope suite, referred to as the RADICALS High Energy Particle Telescope (RADHEPT). This suite further consists of multiple detectors, which are the High Energy Detector, Low Energy Detector and Microburst Detector. The satellite's scientific payload also includes an X-Ray Imager (XRI) to remote sense energetic particle precipitation using back-scattered Bremsstrahlung X-rays, and a boom mounted FluxGate Magnetometer (FGM) and Search Coil Magnetometer (SCM). Simultaneous measurements from RADHEPT, XRI, FGM and SCM aim to provide a unique data product, that aims to improve our understanding of the particle precipitation effects and their underlying causes.

This paper focuses on the design and development of the Microburst Detector, which is one of the instruments to be flown on-board the RADICALS mission. The detector and accompanying signal processing electronics have been designed with a modular architecture enabling use on future CubeSats, Balloons, Sounding Rocket and Small-Satellite missions. In advance of the RADICALS mission, a rendition of the detector has been developed for a sounding rocket test flight from the NASA Wallops Flight Facilities in August 2024. The detector was selected as a part of the *Payload for Energetic Particle Precipitation Education and Research (PEPPER-X)* mission which is the first Canadian student-team payload selected for a flight within the NASA RockSat-X program.

Detector Concept and Design

Based on the science questions pertaining to microbursts described in the previous section, it is clear that a detector designed to measure high energy microbursts must have a broad energy range: 100s keV to a few MeV. In addition, the detector must have a fast response time (on the order of microseconds) to resolve the microbursts. The detector must also be able to measure a large maximum flux as the microburst flux is known to increase an order of magnitude or more above the baseline. Additionally, due to the power, mass, and volume constraints of a small satellite mission, the detector must be compact and have low power consumption. Table 1 summarizes the measurement parameters by previous missions, and proposed measurement goals for the RADICALS mission.

A suitable candidate for developing such a detector is to use a combination of silicon photomultipliers (or multi-pixel photon counter (MPPC)) with a scintillator crystal. Such detectors have previously been used in CubeSat missions for Gamma-ray spectroscopy,[13, 14] since they have very low power con-

Table 1: Previous Microburst measurement parameters and proposed measurement goals for the RADICALS microburst detector

Parameter	Previous Measurement Made		Proposed Goal
Mission	FIREBIRD-II[9]	SAMPEX-HILT[12]	RADICALS
Energy Range	0.2 to 1 MeV, > 1 MeV	> 1 MeV	0.2 to 3 MeV
Energy Resolution	5 channels	N/A	> 8 channels
Time Resolution	18.75 ms	20 ms	10 ms
Field of View	180 (and 45) deg	60 deg	180 deg

sumption, high gain, and fast responsivity. In this study, we extend this detection methodology to the in-situ measurement of energetic electrons in space. Figure 2(a) shows a conceptual schematic of the detector. The detector consists of two main elements: a scintillator crystal and the MPPC. An incoming electron interacts with the scintillator crystal and generates photons. The number of photons generated is proportional to the energy of the incoming electron. These photons are then detected by the multi-pixel photon counter, that generates an output pulse with total charge proportional to the number of photons (i.e., proportional to the the energy of the electron). Thus, by measuring the pulse charge, the energy of the incoming electron can be determined. The output pulse is amplified in a preamplifier-shaper circuit giving an output voltage proportional to the pulse charge. The scintillator crystal is also coated with Aluminum, to reflect back the outward emitted photons towards the MPPC. The crystal is coated with a layer of Parylene to provide protection against moisture and corrosion. Since the MPPC detectors are sensitive to ambient light, a chassis has been designed to ensure that the detectors are light tight.

Figure 2(b) shows the exploded view of the CAD model of the microburst detector in its chassis, with the various components labeled. The detector consists of two scintillator crystals, Cesium Iodide doped with Sodium (CsI(Na)) and Lutetium–yttrium oxyorthosilicate (LYSO). The CsI(Na) Crystal and MPPC is placed on the top to detect incoming electrons. The LYSO crystal is placed inside the detector and is shielded from external electrons through the aluminum chassis and circuit boards, so it will not detect incoming electrons. However, the LYSO crystal contains ^{176}Lu that intrinsically decays and producing a emission spectrum consisting of Beta and Gamma radiation.[15] Thus, by measuring the LYSO self-scintillation spectra, the performance and calibration of the detector and electronics can be validated during flight. The detector chassis also has a protective cover that has a layer of Aluminium foil and a layer of Mylar. The cover ensures thermal stability as well as to protects the scintillator from small orbital debris.

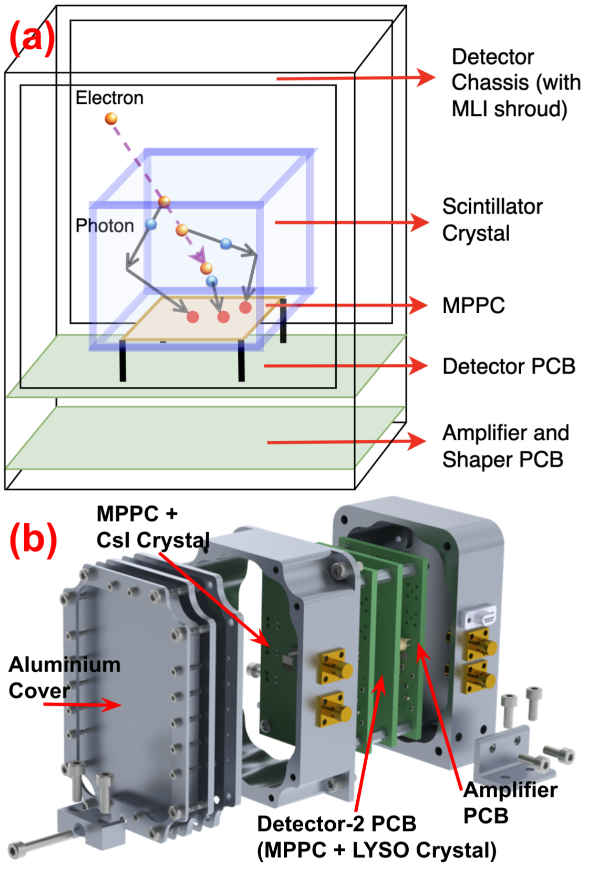

Figure 2: (a) Microburst Detector Concept: The diagram shows a schematic of the detector, that consists of scintillator crystal mounted on a multi-pixel photon counter, an incoming electron generates multiple photons in the scintillator, that are then counted by the multi-pixel photon counter (b) Exploded view of the microburst detector with different components labelled.

Detector Design Trade-offs

In order to design a detector which satisfies the scientific measurement requirements, a number of design parameters need to be optimized. This section describes the computation of the detectors geometric factor, and dependence of maximum measurable flux and energy on the detector's geometric factor.

Geometric Factor

The geometric factor (G) of a particle detector can be defined as factor of proportionality relating the number of particles the detector count rate (C) to the number of particles incident on the detector (the incoming flux, J in units of particles per cm^2 per steradian),

$$C = GJ \tag{1}$$

Due to the the scintillator crystal being a cube, the geometric factor of the detector varies with the angle of incidence of the incoming electrons. The geometric factor at a particular angle of incidence can be calculated based on A_{eff} , which is the 2D projected area of the cube when looking at it from a particular angle. Figure 3 shows a 3D plot of the effective geometric factor for different angles of incidence. From this plot the average geometric factor of the detector can be computed, which is 2.26 cm^2 str for a 0.5 cm size cubic scintillator crystal.

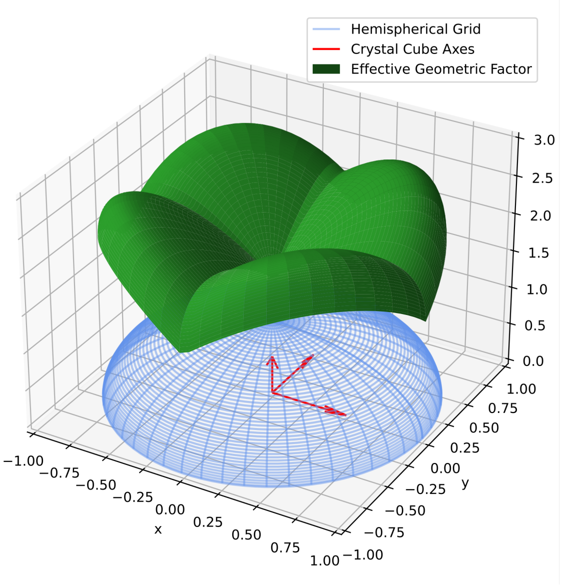

Figure 3: Approximate geometric factor (cm^{2}str) of a 0.5 cm cubic crystal for different angles of incidence of electrons.

Maximum Measurable Flux

As shown in equation 2, the signal in the detector is related to the incoming flux, with the geometric factor as the proportionality constant. Additionally, the maximum count rate depends on the capability of the signal processing electronics system. Figure 4 shows this relation of the maximum measurable flux with the size of the crystal, for four different maximum count rate capabilities of the electronics (which are 100,000 cts/sec (blue), 200,000 cts/sec (red), 500,000 cts/sec (yellow) and 1,000,000 cts/sec (green)). The detector geometric factor for different sized crystal is also plotted on the right hand scale. Based on microburst flux levels observed from previous missions, the maximum integral flux above the minimum energy threshold (200 keV) of the detector is observed to be of the order of $10^5 counts/cm^2/str/sec.$[12] Thus, from the plot a possible solution for this is a 0.5 cm sided cubic crystal with maximum of 200,000 counts/sec (denoted by the intersection of red plot and black dotted line).

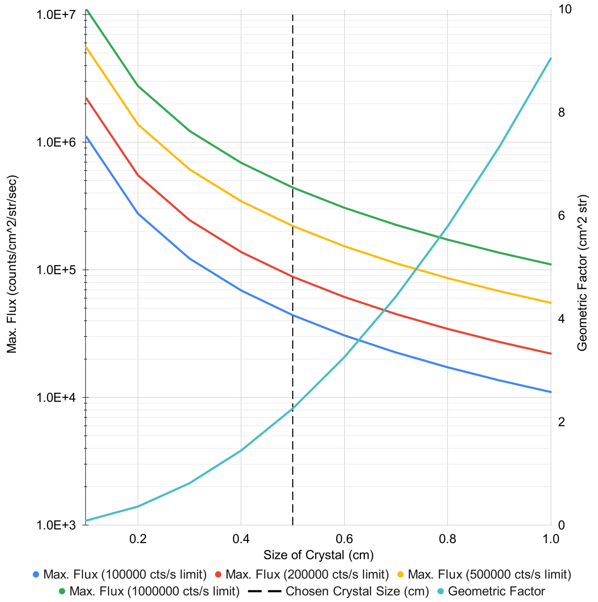

Figure 4: Maximum measurable flux versus size of crystal (cm) for different maximum count rate capabilities of the signal processing electronics.

Maximum Measurable Energy

The maximum measurable energy of an incoming electron depends on the the electron stopping within the length of the crystal, thus depending on the scintillator material properties and the size of the scintillator crystal. The following equation gives the relation between the mean distance travelled by an electron in a material (denoted by Δx or the continuous slowing down approximation (CSDA) range), the initial kinetic energy of the electron E_0, and the linear stopping power of a material $S(E)$,

$$\Delta x = \int_0^{E_0} \frac{1}{S(E)}\, dE \tag{2}$$

Fig 5 shows the variation of maximum measurable energy with respect to the size of the crystal, for a CsI crystal. This has been computed using National Institute of Standards and Technology (NIST) ESTAR program,[16] that contains stopping power of different materials, which can be used to calculate the CSDA range. The plot shows that a 5 mm sized crystal can measure maximum electron energy of approximately 3.5 MeV.

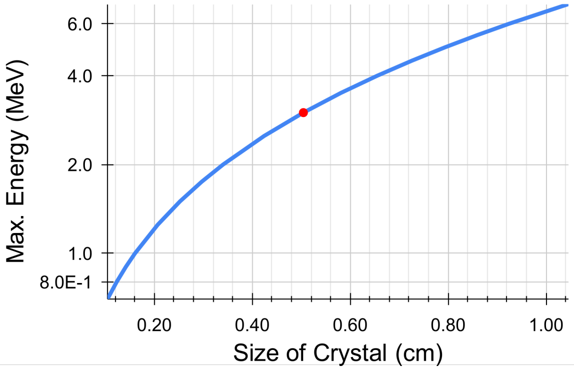

Figure 5: Maximum measurable Energy (MeV) versus size of crystal (cm) for a CsI(Na) scintillator crystal.

Based on the analysis described to determine the maximum measurable flux and maximum measurable energy, it can be seen that a 5 mm sized crystal satisfies the scientific measurement requirements for the both the energy range and incoming flux. This analysis was repeated for different scintillator materials including Bismuth germanate (BGO) and Lutetium–yttrium oxyorthosilicate (LYSO), but is omited here for brevity. Based on this analysis a 5 mm CsI(Na) and a 5mm LYSO crystal was chosen for the sounding rocket test flight detector. The design of the signal processing electronics required to process the detector output signals is described in the next section.

Signal Processing Electronics Design

The overall objective of the instrument is to produce a data product with a histogram of electron counts over the energy range. Figure 6 shows a functional block diagram of the detector and accompanying processing electronics system required to generate such a data product. The analog output signals from the detectors are converted to digital signals, using analog to digital converters (ADC), running at a clock frequency of 25 MHz. The digital signal is then processed by a system on chip (SoC) field programmable gate array (FPGA), that detects the peak height of the pulses, and bins them into appropriate energy channels. This data is then timestamped using a real time counter, and also stored in non-volatile memory on-board. The digital processing electronics then packetizes the data and transfers it to the spacecraft bus for downlinking.

The MPPC detectors require a nominal bias voltage of approximately 55V to operate. In order to generate this voltage, the FPGA also controls a high voltage bias supply of the detectors using digital to analog converters (DAC). The FPGA also monitors the high voltage bias through a feedback network. The temperature of the detector heads are also monitored using thermistors, since the gain of the MPPC detector is dependent on temperature. The various temperatures, voltages and current values are packetized as housekeeping packets and transferred to the spacecraft telemetry bus over a RS232 serial interface. The electronics also includes DC-DC converters to internally generate voltages required for the different electronics components, and the system is designed to run from a single 28V supply.

Prototype Development and realization

Based on the design described in the previous sections, a prototype of the detector and electronics was realized for a test flight on a NASA RockSat-X sounding rocket mission. Both CsI and LYSO detector crystals were included in the design to allow measurements of microburst electrons with the CsI crystal and monitoring of instrument performance and calibration using the self scintillation of the LYSO crystal. Figure 7(a) and (b) shows pictures of the detector taken during flight model assembly. One of the crystals is visible in image (a) and has been coated with aluminium to reflect the scintillation photons inwards. Image (b) shows the two crystals (LYSO and CsI(Na)) during assembly. Image (c) shows the flight model of the detector, that has been covered with the protective aluminium cover. The flight model of the detector head developed for the sounding rocket test flight has a mass of 617 g, and a volume less than 1U. The detector is assembled on a replica of the sounding rocket flight deck, and is connected to the simulated power and telemetry

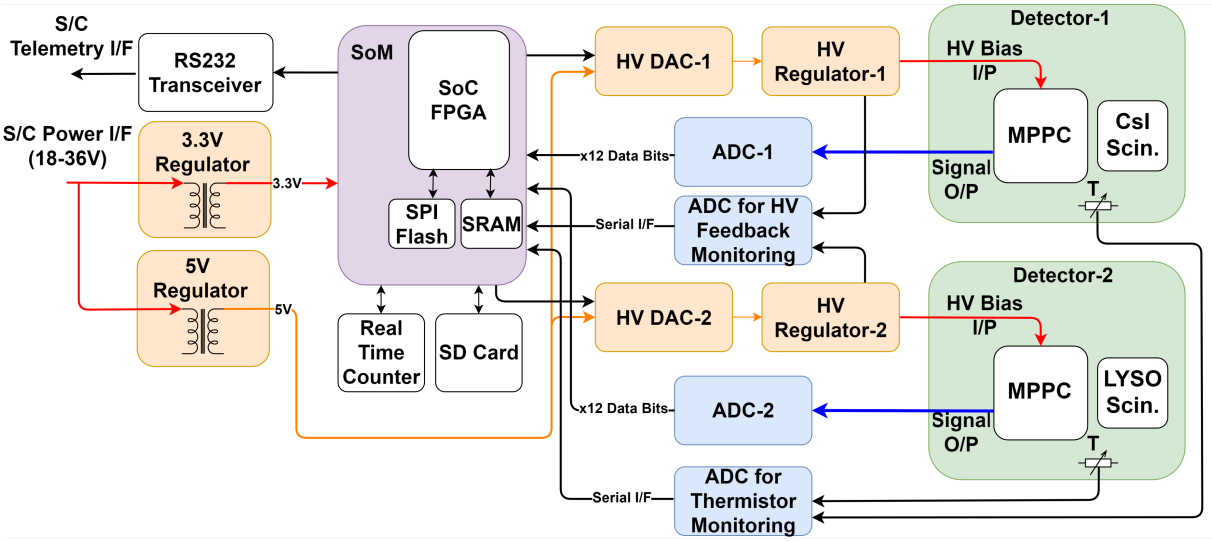

Figure 6: Simplified functional block diagram of the detector and accompanying signal processing electronics system. The spacecraft telemetry and power interfaces are shown on the left, and the scintillator detectors are shown on the right. Red and Orange lines indicate power lines, black arrows indicate digital signals, and blue arrows indicate analog signals.(Acronyms: S/C = Spacecraft, I/F = Interface, SoM = System on Module, SoC = System on Chip, HV = High Voltage, DAC = Digital to Analog Converter, ADC = Analog to Digital Converter)

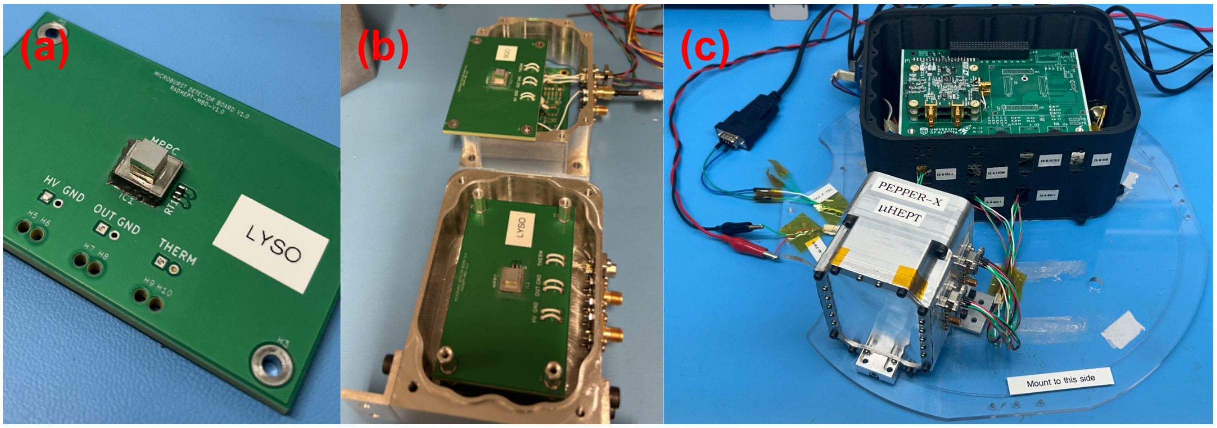

Figure 7: (a) Zoomed-in picture of the crystal and MPPC in the prototype (after aluminium and parylene protective coating is added), (b) The detector prototype during assembly with two scintillator crystals (CsI(Na) and LYSO), (c) The flight model of the detector (with the aluminium protective cover added) and signal processing electronics unit assembled on a replica of the sounding rocket deck.

interface of the rocket. A prototype of the electronics unit is also shown assembled on the deck.

Performance Characterization and Testing

The subsequent subsections describe key tests performed to validate the detector performance with respect to the scientific measurement requirements. These include (a) Dark Noise and Gain characterization, and (b) Calibration with Radioisotope sources. These tests were performed in preparation for the sounding rocket test flight to obtain preliminary calibration results for the detector. The details of the experimental setup and results from these tests are described below.

Dark Noise and Gain Characterization

The multi-pixel photon counter generates an output charge when an incoming photon hits the detector. However, charge pulses are also generated from intrinsic thermally generated carriers, which are called dark pulses. Dark pulses can be generated when one thermally generated Photo-electron triggers one pixel, which are called 1 p.e. pulses. Additionally it is possible that secondary photons are generated in the avalanche process that triggers adjacent pixels. This leads to two photo-electron (2 p.e.) or three photo-electron (3 p.e.) pulses contributing to the dark pulses. These lead to a dark current which can be computed as follows:

$$I_D = qMN_{0.5p.e.}\frac{1}{1 - P_{crosstalk}} \tag{3}$$

where, q denotes the charge of an electron, M is the gain of the MPPC, $N_{0.5p.e.}$ is the dark count rate which is defined as the number of pulses generated in a dark state that cross the threshold of 0.5 p.e., and $P_{crosstalk}$ denotes the probability of crosstalk happening. $N_{0.5p.e.}$ and $P_{crosstalk}$ can be computed as follows:

$$N_{0.5p.e.} = AT^{\frac{3}{2}}e^{\frac{-E_g}{2kT}} \tag{4}$$

$$P_{crosstalk} = \frac{N_{1.5p.e.}}{N_{0.5p.e.}} \tag{5}$$

Here T is the absolute temperature (in Kelvin), A is a arbitrary constant, E_g is the band gap energy (1.12 eV for the silicon detectors used in this study), k is the Boltzamn constant (eV/K), and $N_{1.5p.e.}$ is the number of pulses generated in a dark state that cross the threshold of 1.5 p.e. By measuring the dark current at a given temperature and a knowledge of the self breakdown rate, the gain of the MPPC can be determined as a function of voltage.

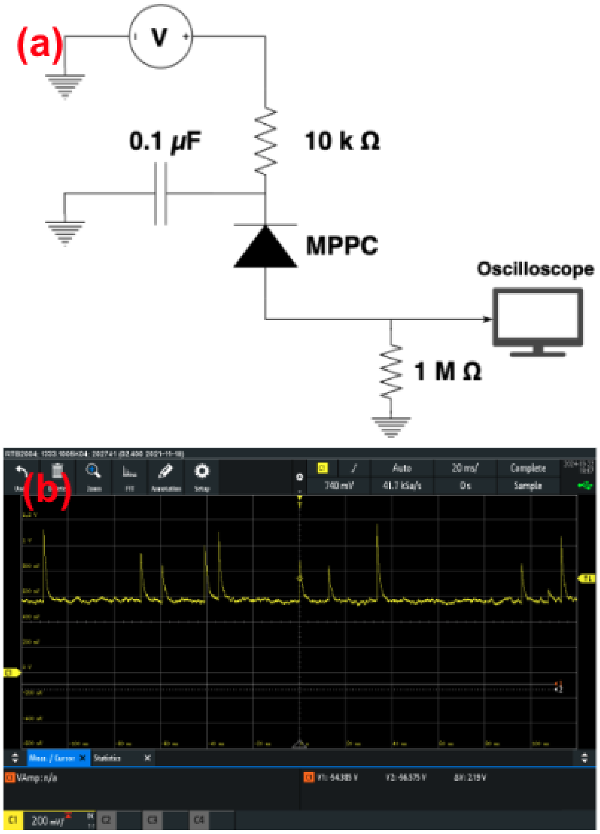

Figure 8: (a) Detector dark noise characterization test setup, (b) Oscilloscope output from the MPPC with the LYSO Crystal. The baseline (approx. 580 mV) denotes the dark current, and actual LYSO self-scintillation pulses are seen at various random times.

Figure 8(a) shows the test setup schematic. The left panel shows the circuit where the detector is connected to a oscilloscope with a 1 MΩ input resistance. A bias voltage is applied to the detector that is 3V above the breakdown voltage (as recommended by the manufacturer). The MPPCs chosen in this detector (Hamamatsu S13360-6075CS[?]) have a pixel pitch of 75 micrometers, and correspondingly the typical dark count rate given by the manufacturer is approximately 2000 kcps at 25 Celsius and the crosstalk probability is 7 percent. The oscilloscope outputs are shown in figure 8 showing the leakage current for the LYSO detector. Actual scintillation spikes are seen randomly in time due to self-scintillation of ^{176}Lu, which is a natural isotope of Lutetium. The voltage in both oscilloscope traces across the 1 MΩ input resistance is 580 mV, which implies that the leakage current is,

$$I_D = \frac{V_{scope}}{1M\Omega} \approx \frac{580mV}{1M\Omega} \approx 0.58\mu A \tag{6}$$

Then, the gain of the MPPC can be calculated using equation 3,

$$M = \frac{I_D}{qMN_{0.5p.e.}\frac{1}{1-P_{crosstalk}}} \tag{7}$$

$$M \approx \frac{0.58 * 10^{-6}}{1.602 * 10^{-19} * 2000 * 10^{3} * \frac{1}{1-0.07}} \approx 1.68 * 10^{6} \tag{8}$$

This value is reasonably close to the expected value provided by the manufacturer, which is typically stated as $4.0 * 10^6$. The difference in the measurement could be attributed to the approximations made in the dark count rate, as well as differences in breakdown voltage in different MPPC detectors.

Radio-isotope Calibration Experiments

In this test the detector is exposed to different radioisotope sources. Since the spectrum of the sources are known, the detector output response can be compared to the source spectrum to obtain calibration results for the detector. The detector is connected to a bias supply, and the radiation source is placed near the detector. The output of the detector is connected to an oscilloscope to monitor and store the output pulses. The output pulses are then binned and a histogram plot is created of the emission spectrum. The subsequent subsections show preliminary calibration results from the LYSO self emission spectrum and Strontium-90 radioisotope source.

LYSO Self Emission Spectra

Figure 9 shows the measured spectrum of the LYSO self-scintillations. The measured spectrum using the detector includes a histogram as well as a smoothed curve generated using kernel density estimation. The kernel density estimate is calculated as follows:

$$f_h(x) = \frac{1}{nh}\sum_{i=1}^{n}\frac{K(x - x_i)}{h} \tag{9}$$

where, $x_i \ldots x_n$ are the n histogram data sample points, K is the Gaussian kernel function, and h is the smoothing parameter.

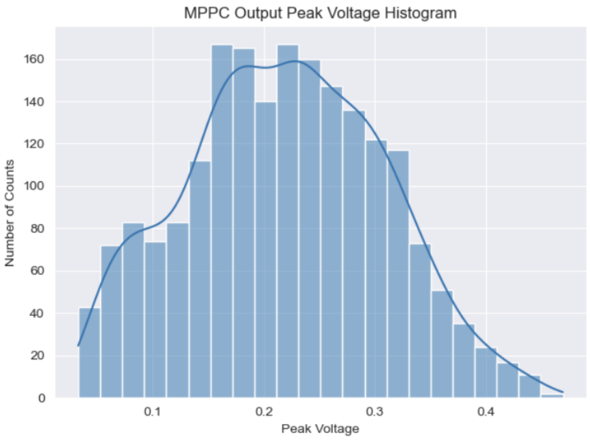

Figure 9: Histogram of measured pulse height spectrum for LYSO self-scintillation

Strontium-90 Beta Decay Spectra

Figure 10 shows the Strontium source electron energy spectrum measured by the detector. The output spectrum is shown in detector bins that are obtained form the FPGA, after peak finding and binning the pulses. The test was performed by inserting different thicknesses of alumium filters, to attenuate the electrons. This can be seen in the detector response, with decreasing counts as more aluminum thickness is added.

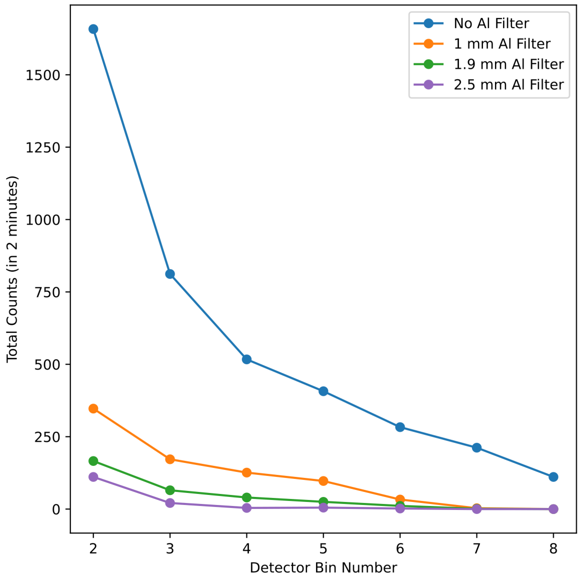

Figure 10: Histogram of measured pulse height signals for Sr-90 sources detected with the CsI(Na) crystal

Other radio-isotope calibration tests with Barium (Ba-133) and Cobalt (Co-60) have been performed on the detector but are omitted here for brevity. Based on these tests, and by comparing the measured LYSO spectrum, to the known self-scintillation spectrum[15] a preliminary calibration of LYSO scintillation crystal can be obtained as 2 keV/mv. Further analysis of the radio-isotope calibration measurement data is being conducted to obtain more accurate calibration coefficient and error-bars for both the LYSO and CsI(Na) detectors.

Discussion and Conclusion

In this study, a novel approach to measuring electron microbursts in satellite missions using scintillators coupled to Silicon photomultiplier detectors was proposed and initial operation demonstrated. A complete detector system with FPGA signal processing was developed for an upcoming sounding rocket test flight. It was demonstrated that this new approach has a scalable geometric factor, adequate sensitivity to cover the required electron energy detection range and is also capable of high count rates upto 200 kcps. Overall, the work done in this study paves the way for flying such detectors on future CubeSat and Small-satellite missions. The instrumentation developed during this study will enable high-fidelity in-situ energetic electron measurements that in-turn will improve our understanding of energetic electron precipitation and radiation belt dynamics.

Future Work

In order to calibrate the detector more accurately, further radio-isotope and beamline experiments will be performed. Additionally, to get a more accurate estimate of detector geometric factor and performance for electrons arriving at different angles, detailed Monte-Carlo simulations of the detector must be completed. For the signal conditioning electronics, the current detector has been realized using COTS components, a future version can be realized using rad-hard components for use in harsher radiation environments beyond the low-Earth orbit. These additional improvements and calibrations will be carried out in order to prepare the detector for the upcoming RADICALS mission.

Acknowledgments

We thank the various staff and students at the University of Alberta involved in the development of the RADICALS and PEPPER-X missions. We gratefully acknowledge that the RADICALS mission is funded through grants from the Canadian Space Agency, Canadian Foundation of Innovation, and the Government of Alberta. We thank the NASA RockSat-X program for providing sounding rocket launch support for PEPPER-X. This work is also supported by research grants from the National Sciences and Engineering Research Council of Canada (NSERC) to Ian R. Mann and Robert Fedosejevs (RGPIN-2019-05013), by the NSERC CREATE for International Space Mission Training program, and the Canadian Space Agency.

References

[1] N. Y. Ganushkina, I. Dandouras, Y. Y. Shprits, and J. Cao, "Locations of boundaries of outer and inner radiation belts as observed by Cluster and Double Star," *Journal of Geophysical Research: Space Physics*, vol. 116, no. A9, 2011. [Online]. Available: https://onlinelibrary.wiley.com/doi/abs/10.1029/2010JA016376

[2] S. Kanekal, D. Baker, and D. Sibeck, "Recent advances in our understanding of the Earth's Radiation Belts," in *2019 International Conference on Electromagnetics in Advanced Applications (ICEAA)*. Granada, Spain: IEEE, Sep. 2019, pp. 1345–1348. [Online]. Available: https://ieeexplore.ieee.org/document/8879310/

[3] R. Vainio, L. Desorgher, D. Heynderickx, M. Storini, E. Flückiger, R. B. Horne, G. A. Kovaltsov, K. Kudela, M. Laurenza, S. McKenna-Lawlor, H. Rothkaehl, and I. G. Usoskin, "Dynamics of the Earth's Particle Radiation Environment," *Space Science Reviews*, vol. 147, no. 3, pp. 187–231, Nov. 2009. [Online]. Available: https://doi.org/10.1007/s11214-009-9496-7

[4] J. A. Van Allen, G. H. Ludwig, E. C. Ray, and C. E. McILWAIN, "Observation of High Intensity Radiation by Satellites 1958 Alpha and Gamma," *Journal of Jet Propulsion*, vol. 28, no. 9, pp. 588–592, Sep. 1958, publisher: American Institute of Aeronautics and Astronautics. [Online]. Available: https://arc.aiaa.org/doi/10.2514/8.7396

[5] R. A. Marshall and C. M. Cully, "Chapter 7 - Atmospheric effects and signatures of high-energy electron precipitation," in *The Dynamic Loss of Earth's Radiation Belts*, A. N. Jaynes and M. E. Usanova, Eds. Elsevier, Jan. 2020, pp. 199–255. [Online]. Available: https://www.sciencedirect.com/science/article/pii/B978012813371200007X

[6] J. C. Chancellor, G. B. I. Scott, and J. P. Sutton, "Space Radiation: The Number One Risk to Astronaut Health beyond Low Earth Orbit," *Life : Open Access Journal*, vol. 4, no. 3, pp. 491–510, Sep. 2014. [Online]. Available: https://www.ncbi.nlm.nih.gov/pmc/articles/PMC4206856/

[7] S. S. Elliott, A. Breneman, C. Colpitts, J. Bortnik, A. Jaynes, A. Halford, M. Shumko, L. Blum, L. Chen, A. Greeley, and D. Turner, "Understanding the properties, wave drivers, and impacts of electron microburst precipitation: Current understanding and critical knowledge gaps," *Frontiers in Astronomy and Space Sciences*, vol. 9, 2022. [Online]. Available: https://www.frontiersin.org/articles/10.3389/fspas.2022.1062422

[8] R. M. Millan, M. P. McCarthy, J. G. Sample, D. M. Smith, L. D. Thompson, D. G. McGaw, L. A. Woodger, J. G. Hewitt, M. D. Comess, K. B. Yando, A. X. Liang, B. A. Anderson, N. R. Knezek, W. Z. Rexroad, J. M. Scheiman, G. S. Bowers, A. J. Halford, A. B. Collier, M. A. Clilverd, R. P. Lin, and M. K. Hudson, "The Balloon Array for RBSP Relativistic Electron Losses (BARREL)," *Space Science Reviews*, vol. 179, no. 1, pp. 503–530, Nov. 2013. [Online]. Available: https://doi.org/10.1007/s11214-013-9971-z

[9] A. B. Crew *et al.*, "First multipoint in situ observations of electron microbursts: Initial results from the NSF FIREBIRD II mission," *Journal of Geophysical Research: Space Physics*, vol. 121, no. 6, pp. 5272–5283, 2016. [Online]. Available: https://onlinelibrary.wiley.com/doi/abs/10.1002/2016JA022485

[10] M. Shumko *et al.*, "Electron Microburst Size Distribution Derived With AeroCube-6," *Journal of Geophysical Research: Space Physics*, vol. 125, no. 3, p. e2019JA027651, 2020. [Online]. Available: https://onlinelibrary.wiley.com/doi/abs/10.1029/2019JA027651

[11] D. Mourenas, A. V. Artemyev, X. J. Zhang, V. Angelopoulos, E. Tsai, and C. Wilkins, "Electron Lifetimes and Diffusion Rates Inferred From ELFIN Measurements at Low Altitude: First Results," *Journal of Geophysical Research: Space Physics*, vol. 126, no. 11, p. e2021JA029757, 2021. [Online]. Available: https://onlinelibrary.wiley.com/doi/abs/10.1029/2021JA029757

[12] C. Meyer-Reed, L. Blum, and M. Shumko, "Pitch Angle Isotropy of Relativistic Electron Microbursts as Observed by SAMPEX/HILT: Statistical and Storm-Time Properties," *Journal of Geophysical Research: Space Physics*, vol. 128, no. 1, p. e2022JA030926, 2023. [Online]. Available: https://onlinelibrary.wiley.com/doi/abs/10.1029/2022JA030926

[13] A. Pál *et al.*, "GRBAlpha: a 1U CubeSat mission for validating timing-based gamma-ray burst localization," in *Space Telescopes and Instrumentation 2020: Ultraviolet to Gamma Ray*, vol. 11444. SPIE, Dec. 2020, pp. 825–833. [Online]. Available: https://www-spiedigitallibrary-org.login.ezproxy.library.ualberta.ca/conference-proceedings-of-spie/11444/114444V/GRBAlpha--a-1U-CubeSat-mission-for-validating-timing-based/10.1117/12.2561351.full

[14] N. Werner *et al.*, "CAMELOT: Cubesats Applied for MEasuring and LOcalising Transients mission overview," in *Space Telescopes and Instrumentation 2018: Ultraviolet to Gamma Ray*, vol. 10699. SPIE, Jul. 2018, pp. 672–686. [Online]. Available: https://www.spiedigitallibrary.org/conference-proceedings-of-spie/10699/106992P/CAMELOT--Cubesats-Applied-for-MEasuring-and-LOcalising-Transients-mission/10.1117/12.2313764.full

[15] H. Alva-Sánchez, A. Zepeda-Barrios, V. D. Díaz-Martínez, T. Murrieta-Rodríguez, A. Martínez-Dávalos, and M. Rodríguez-Villafuerte, "Understanding the intrinsic radioactivity energy spectrum from 176Lu in LYSO/LSO scintillation crystals," *Scientific Reports*, vol. 8, no. 1, p. 17310, Nov. 2018, publisher: Nature Publishing Group. [Online]. Available: https://www.nature.com/articles/s41598-018-35684-x

[16] H. Bichsel, "Stopping power of fast charged particles in heavy elements," Jan. 1991, national Institute of Standards and Technology, Gaithersburg, MD. [Online]. Available: https://doi.org/10.6028/NIST.IR.4550